Chinese Chemical Letters 36 (2025) 110922

Contents lists available at ScienceDirect

Chinese Chemical Letters

journal homepage: www.elsevier.com/locate/cclet

Harnessing the interfacial sulfur-edge and metal-edge sites in $ZnIn_2S_4$/MnS heterojunctions boosts charge transfer for photocatalytic hydrogen production

Yueting Ma[a,b], Zhiyan Feng[b], Yuxin Dong[a], Zhiyong Yan[a], Hou Wang[b,*], Yan Wu[a,*]

[a] College of Environment and Ecology, Hunan Agricultural University, Changsha 410128, China
[b] Key Laboratory of Environment Biology and Pollution Control, College of Environmental Science and Engineering, Hunan University, Changsha 410082, China

ARTICLE INFO

Article history:
Received 6 December 2024
Revised 27 January 2025
Accepted 5 February 2025
Available online 5 February 2025

Keywords:
$ZnIn_2S_4$/MnS
S-scheme
Photocatalysis
M-S bonds

ABSTRACT

Rapid carrier recombination and slow charge transfer dynamics have significantly reduced the performance of photocatalytic hydrogen production. Construction of heterojunctions *via* utilizing the sulfur-edge and metal-edge sites of metal sulfide semiconductor for improving photocatalytic activity remains a significant challenge. Herein, a novel $ZnIn_2S_4$/MnS S-scheme heterojunction was prepared by hydrothermal synthesis to accelerate charge carrier transfer for efficient photocatalysis. Notably, $ZnIn_2S_4$/MnS exhibited excellent photocatalytic hydrogen evolution activity (7.95 mmol g^{-1} h^{-1}) under visible light irradiation (≥420 nm), up to 4.7 times higher than that of pure $ZnIn_2S_4$. Additionally, cycling experiments showed that ZM-2 remained high stability after four cycles. Density-functional theory (DFT) calculations and *in situ* XPS results confirm the formation of S-scheme heterojunction, indicating that the tight interfacial contact between $ZnIn_2S_4$ and MnS with the presence of Mn-S bonds (the unsaturated Mn edges of MnS and the uncoordinated S atoms in the edge of $ZnIn_2S_4$) promoted faster charge transfer. Besides, the unsaturated S atom on the surface of MnS is an active site with strong H^+ binding ability, which can effectively reduce the overpotential or activation barrier for hydrogen evolution. This study illustrates the critical influence of the interfacial Mn-S bond on the $ZnIn_2S_4$/MnS S-scheme heterojunction to achieve efficient photocatalytic hydrogen production and provides relevant guidance for carrying out rational structural/interfacial modulation.

Energy shortages and environmental pollution are driving the search for cleaner energy sources. There is currently a looming need to address the shortage of energy supply due to the poor regenerative capacity of conventional energy sources [1]. Compared to traditional energy sources, hydrogen has a high specific energy value and a clean by-product, which is one of the most promising fuels [2,3]. However, inefficient and energy-intensive hydrogen production technologies severely limit the utilization of hydrogen energy now. Among many hydrogen production technologies, photocatalytic water separation is a very promising technology for producing hydrogen, as it has the advantages of environmentally friendly and low energy consumption [4–6]. In the past decades, photocatalytic hydrogen production mainly focused on various photocatalytic systems, including metal oxides, metal sulfides, two-dimensional materials, metal-organic frameworks and their derived nanomaterials. Among these, metal sulfides exhibited the excellent ability to utilize solar energy more efficiently due to their tunable band gaps. Up to now, quite a limited strategy has been proposed for simultaneous regulation of electronic structure and interfacial reaction from the views of the sulfur-edge and metal-edge sites in the solid-liquid interface.

As a typical ternary layered metal sulfide semiconductor, $ZnIn_2S_4$ has been widely explored by researchers for its tunable bandgap and low toxicity [7–11]. Nevertheless, individual $ZnIn_2S_4$ is largely hindered by the large amount of photo corrosion induced by photoexcited holes, making it not so desirable as a photocatalyst [12,13]. In the pursuit of higher $ZnIn_2S_4$ photocatalytic activity, researchers have made many attempts such as elemental doping [14,15], defect engineering [16], and heterostructure construction [17–20]. MnS as a transition metal sulfide material has been applied widely in optoelectronic devices and supercapacitors, for its rich natural reserves, environmental friendliness and high

* Corresponding authors.
E-mail addresses: wangh@hnu.edu.cn (H. Wang), wu_yan@hunau.edu.cn (Y. Wu).

https://doi.org/10.1016/j.cclet.2025.110922
1001-8417/

light-absorbing capacity [21]. The photocatalytic ability of MnS were rarely attracted attention due to its insufficient photocatalytic activity [22]. The formation of heterojunction can inhibit the electron-hole complexation in the photocatalyst [23,24]. It is expected that the photocatalytic ability of MnS and the photo corrosion of $ZnIn_2S_4$ can be improved after the formation of heterojunction between MnS and $ZnIn_2S_4$. It is also crucial to study the carrier separation and transfer mechanisms and how to accelerate the process, which can be achieved by constructing interfacial chemical bonds between materials as direct electron transfer channels. For example, Zhu *et al.* exploited the ultrafast carrier dynamics triggered by Ga-S bonds in GaZnON/CdS heterojunction for efficient photocatalytic hydrogen production [25]. Based on heterojunction engineering, MnS was combined with $ZnIn_2S_4$ to explore the interfacial effects of its composite structure. Besides, heterojunctions can contribute more exposed active sites and promote the reaction kinetics [26]. The most common heterojunction in composites is the type II heterojunction, which spatially separates photogenerated charges. Nevertheless, the redox capacity of the charge carriers is significantly reduced due to the transfer of electrons and holes from the type II heterojunction to their corresponding lower energy bands [27]. The energy band configuration of the S-scheme heterostructure is identical to that of the type II heterostructure, but it offers notably distinct electron transfer pathways that enhance charge separation and maintain a high redox potential for effective photocatalysis [28,29]. Typically, active sites of metal-sulfide photocatalysts can be classified as S-edge sites, metal-edge sites, terrace sites, defects, and vacancies [22]. Edge sites are those on the edge, whereas terrace sites lie at the basal plane of the particle. Generally, the active catalytic sites of metal sulfides are situated in the metal-edge sites, Sedge sites, and defects, whereas those in the basal plane are catalytically inert. To the best of our knowledge, there are no reports about the regulation of the sulfur-edge and metal-edge sites *via* the formation of metal sulfide heterojunctions.

In this study, we successfully synthesized a novel $ZnIn_2S_4$/MnS nanoflower S-scheme heterojunction photocatalyst using eutectic and hydrothermal methods (Fig. 1). In order to regulate the interfacial effect of heterojunctions, we prepared composites with different ratios by adding different masses of MnS and used them for photocatalytic hydrogen production under visible light irradiation (≥420 nm). The carrier separation efficiency is greatly improved because of the presence of the built-in electric field and the interfacial Mn-S bond as a direct electron transfer channel. Thus, the prepared material exhibits significantly higher photocatalytic hydrogen production activity of 7.95 mmol g^{-1} h^{-1}, up to 4.7 times higher than that of $ZnIn_2S_4$ (ZIS). In this work, $ZnIn_2S_4$/MnS S-scheme heterojunctions featuring interfacial Mn-S bonds were innovatively fabricated, as well as probed the optimal reactive sites

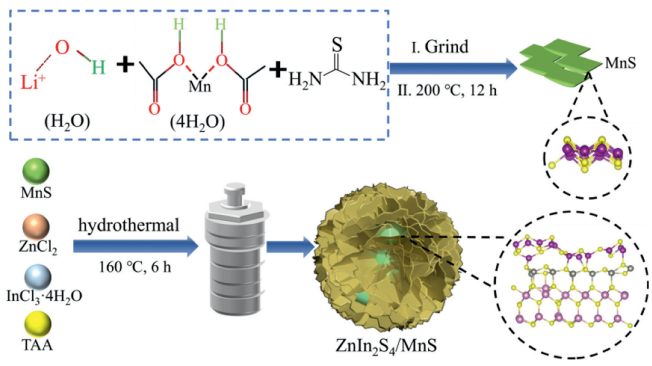

Fig. 1. Synthesis diagram of $ZnIn_2S_4$/MnS heterojunctions.

within this reaction system and had understanding of the transfer mechanism of photogenerated carriers.

The crystal structure of ZIS and MnS nanosheets were investigated using X-ray diffraction (XRD) (Fig. S1 in Supporting information). The primary diffraction peaks for ZIS are associated with hexagonal ZIS (PDF #72–0773) [30]. At 29.6°, 34.6°, 49.6°, 61.7°, and 72.6°, MnS exhibits diffraction peaks simultaneously that agree with the facets of (111), (200), (220), (222), and (400) of α-MnS (PDF #88–2223) [31]. The crystallinity of the composites obtained after loading ZIS on MnS is weakened. The XRD spectra of $ZnIn_2S_4$/MnS-X (ZM-X, X = 1, 2, 3, 4) showed weak characteristic peaks ((200) and (220)) of MnS, which is due to MnS is encased inside the ZIS [32]. Besides, in the ZM-X series samples, the intensity of the peaks related to ZIS decreased, such as (006), (102) and (110), which implies an increase in the MnS content. The photocatalytic activity of the four materials varied, which may be due to the different amounts of MnS.

To study the morphology of the materials, they were analyzed using scanning electron microscope (SEM). From Fig. 2a, MnS comprises stacked nanosheets with an average length of 100–300 nm, which were smaller in size compared to ZIS. ZIS exhibits a nanoflower-like shape composed of many nanosheets (Fig. 2b). The morphological features of ZM-2 are similar to ZIS, which is also a nanoflower-like morphology formed by the stacking of nanosheets (Fig. 2c), MnS dispersed in ZIS nanoflowers. Because of the intimate contacts between the heterostructures, ZM-2 nanosheets have a larger pitch and fewer layers, which both reduces the aggregation of ZIS nanosheets and promotes interface electron transport [33].

To further investigate the interfacial relationship between MnS and ZIS, the transmission electron microscope (TEM) analysis was performed. In Fig. 2d, it can be noticed that ZM-2 is an ultrathin two-dimensional structure composed of intersecting nanosheets. Two different types of lattice stripes are able to be seen, which are crossed in Fig. 2e. From the fast Fourier transform (FFT) and inverse FFT (IFFT) images (Figs. 2f and g), the interplanar spacing of 0.18 nm and 0.32 nm can be assigned to the (220) and (102) planes of MnS and ZIS [31,34], respectively, verifying the heterogeneous nature and high crystallinity of ZM-2. It corroborates with previous XRD results. The energy dispersive spectrometer (EDS) elemental analysis can be seen in Figs. 2h–l, the S, In and Zn elements are equally and intensely distributed in the composites, while the Mn element is quite sparse. This means that the $ZnIn_2S_4$/MnS has been successfully prepared.

Determination of elemental composition of materials was obtained using X-ray photoelectron spectroscopy (XPS). In Fig. S2a (Supporting information), the survey spectrum revealed that Zn, In, S and Mn elements derived from ZIS and MnS coexist in ZM-2, suggesting that ZIS and MnS have been combined successfully. Zn 2p in the pure ZIS was found to have two peaks in its high-resolution spectra (Fig. S2b in Supporting information) at 1022.3 and 1045.3 eV, respectively, related to Zn $2p_{3/2}$ and Zn $2p_{1/2}$ [35]. The binding energy peaks of In^{3+} for In 3d in ZIS were located at 445.2 and 452.7 eV (Fig. S2c in Supporting information), corresponding to the orbitals of In $3d_{5/2}$ and In $3d_{3/2}$, respectively [36]. In Fig. S2d (Supporting information), two Mn peaks at 653.1 and 641.6 eV can be identified in the MnS spectrum as Mn $2p_{1/2}$ and $2p_{3/2}$, respectively. Due to encapsulation by ZIS, the peak intensity of Mn 2p attributed to MnS in ZM-2 is greatly attenuated compared to that of pure MnS peaks [37]. In addition, S 2p in ZIS shows two fitted peaks (Fig. S2e in Supporting information) at 161.9 and 163.3 eV, which corresponds to the S $2p_{1/2}$ and S $2p_{3/2}$ orbitals. After coupling with ZIS, a slight negative shift of the peaks of Mn can still be seen in Fig. S2d, implying that MnS and ZIS in the composite are interacting to affect the electron transfer. However, the peaks of Zn 2p (1022.2 and 1045.2 eV), In 3d (445.1 and

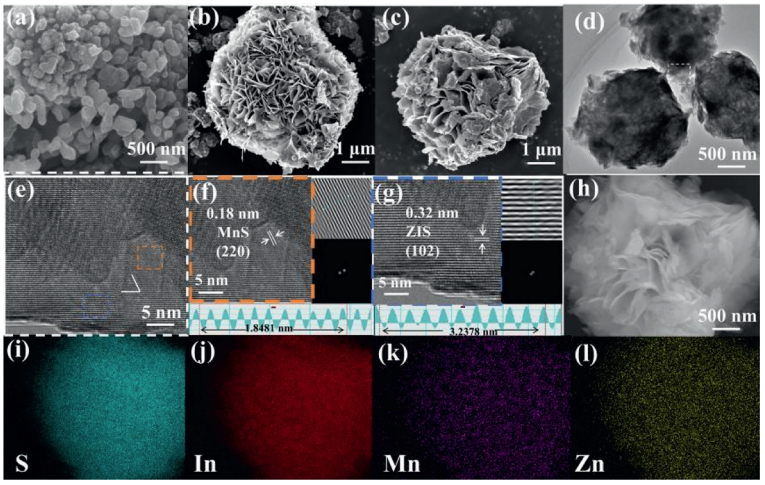

Fig. 2. SEM images of (a) MnS, (b) ZIS and (c) ZM-2. (d) TEM image of ZM-2. (e-g) HRTEM images of ZM-2. (h-l) High-magnification SEM-EDS mappings of ZM-2.

452.6 eV) and S 2p (161.8 and 163.0 eV) showed a slight positive shift in the ZM-2 material as compared to pure ZIS. It indicated that in ZM-2 the electron migration from MnS to ZIS [38]. Heterostructure can change the electron density around atoms [39]. According to the results of XPS analysis, it can be seen that the composite was effectively prepared and there was an interaction between ZIS and MnS. The heterogeneous interfaces *via* the combination of the unsaturated Mn edges of MnS and the uncoordinated S atoms in the edge of ZIS can generate electronic coupling and interfacial synergistic effects, which contribute to the enhancement of structural stability and rapid photogenerated charge carrier transfer/separation. At the same time, it can establish electron transport channels to strengthen the spatial separation of photogenerated charges and increase more opportunities for photogenerated electrons to act in photocatalytic water splitting [40].

The photocatalytic performances of the catalysts in visible light were tested with the sacrificial reagent (thioacetamide, TEOA) and co-catalyst (Pt). We performed some comparative experiments to improve the optimization of the hydrogen production system. In the absence of TEOA or Pt co-catalysts, little H_2 was generated (Fig. 3a). When ZM-2 is not added to the system, only the co-catalyst Pt and the sacrificial agent TEOA are not significant products. Also, no apparent product was noticed in the experiments carried out in the absence of light conditions, which demonstrates the significance of each factor in the photocatalytic reaction. The photocatalytic hydrogen evolution rates of ZM-1, ZM-2, ZM-3, ZM-4 and ZIS are 1.71, 5.95, 5.04, 3.30 and 1.68 mmol g^{-1} h^{-1} (Fig. 3b), respectively, and the ZM-2 exhibited the best performance, with 3.5 times the H_2 production activity of ZIS. Compared with the published literature, especially the works with the catalysts centered on ZIS, the hydrogen production rate of ZM-2 prepared in this paper is significantly better than that of the related catalyst (Fig. S3 and Table S1 in Supporting information). In order to evaluate the stability of composites and their potential practical applications, the stability of ZM-2 was tested in four consecutive tests under the conditions of 10% TEOA and 2 wt% Pt. The hydrogen release activity of ZM-2 showed no significant decline over 16 h (Fig. 3c). As shown in Fig. S4 (Supporting information), the hydrogen production rate of ZM-2 barely decreased during the 12-h continuous hydrogen production experiment. Compared with $TiO_2/ZnIn_2S_4$, $ZnIn_2S_4/BiVO_4$, $ZnIn_2S_4/g\text{-}C_3N_4$, it has better stability [41–43]. In addition, Fig. 3d and Fig. S5 (Supporting information) show the XRD and XPS characterization of ZM-2 before and after four consecutive cycles, respectively. The XRD results indicating that the crystal structure and surface chemical state of ZM-2 did not change after the photocatalytic reaction. And the peak binding energy position in XPS did not change after reaction, indicating that there was no significant change in the surface chemical state of the photocatalyst before and after reaction. The above results indicate that ZM-2 has excellent stability in photocatalysis. Fig. S6 (Supporting information) shows the UV–vis absorption spectrum of ZM-2 sample and the apparent quantum yield (AQY) of photocatalytic H_2 production based on ZM-2 sample as a function of incident light wavelength. The results showed that the highest AQY of ZM-2 samples was 3.2% at 420 nm wavelength.

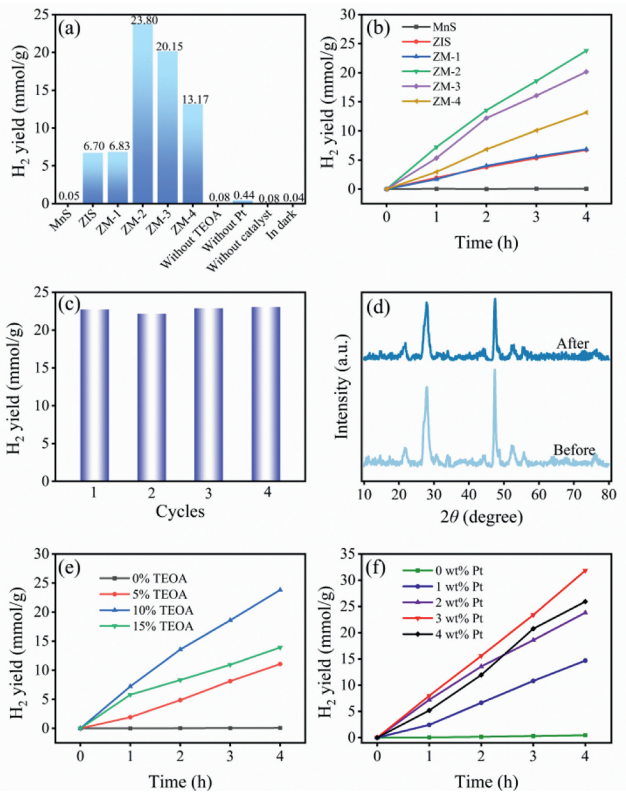

Fig. 3. (a) Hydrogen production activity under various conditions. (b) Production of hydrogen with time over MnS, ZIS and ZM-X samples under visible light. (c) Production of hydrogen by the ZM-2 sample exposed to visible light for four cycles. (d) XRD patterns of ZM-2 prior to and following the photocatalytic reaction. Influence of various concentrations of sacrificial agent TEOA (e) and co-catalyst Pt (f) on ZM-2 photocatalytic hydrogen production.

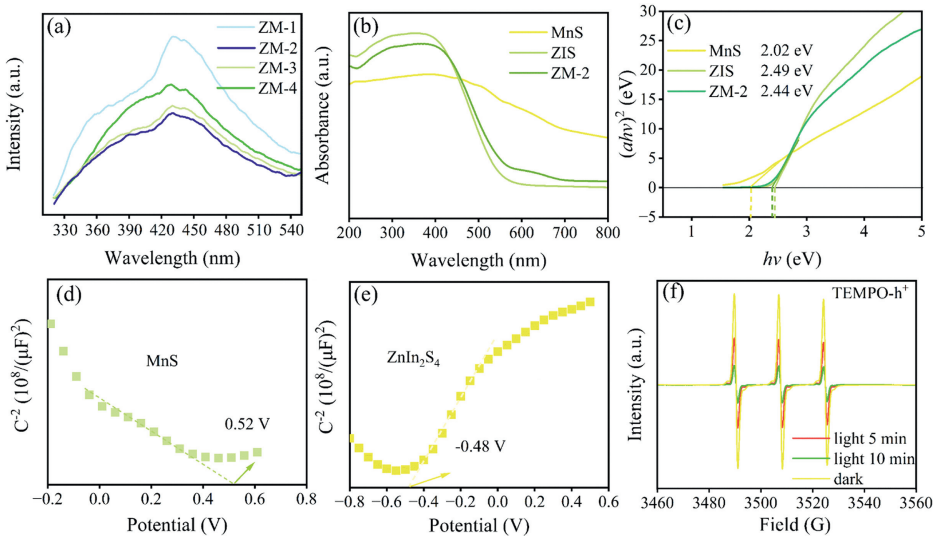

Fig. 4. (a) PL spectra of ZM-X (X = 1,2,3,4). (b) Diffuse reflectance spectra in UV–vis. (c) Plot of $(\alpha h\nu)^2$ *vs.* $h\nu$ (photon-energy) of MnS, ZIS and ZM-2. (d) M-S plots of MnS. (e) M-S plots of ZIS. (f) ESR spectra of TEMPO-h$^+$.

The hydrogen production performance of ZM-2 has been optimized by different concentrations of TEOA. As can be seen from Fig. 3e, the hydrogen evolution of ZM-2 increased when the content of TEOA was between 0 and 10%. However, the production of hydrogen decreased when the TEOA content was raised to 15%. That is due to the fact that TEOA is an organic amine that can also be used as a reducing agent to avoid carriers recombination, but its solubility is limited and may form aggregates on the surface of the photocatalyst, contributing to reduced photocatalytic activity [44]. In addition, Pt nanoparticles enhance H_2 photo-generation by providing abundant active sites. The amount of co-catalyst Pt was also optimized and the results were shown in Fig. 3f. The hydrogen production improved with the mass fraction of Pt in the range of 0–3 wt%, and the hydrogen production rate of ZM-2 decreased at a mass fraction of 4 wt%, which may be attributed to the excessive loading of Pt covering its light absorption sites [45]. Therefore, in this work, the optimal hydrogen production (7.95 mmol g^{-1} h^{-1}) was attained with a 10 vol% TEOA addition and a 3 wt% Pt photodeposition.

The charge-transfer properties of ZIS, MnS and ZM-2 sample were investigated by the transient photocurrent measurement and Nyquist plots. From Fig. S7a (Supporting information), ZM-2 exhibited the highest photoelectric current under alternating xenon lamp light irradiation, suggesting that the combination of ZIS and MnS mitigated the recombination process of charge carriers, enhanced the photoelectric conversion efficiency, and prolonged the charge lifetime (Fig. S7a). Similar results were observed in electrochemical impedance spectroscopy (EIS) (Fig. S7b in Supporting information). ZM-2 complexes have a smaller arc radius than pure ZIS and MnS. In the Nyquist figure, smaller arc radius often corresponds to lower interfacial resistance and higher charge transfer efficiency [46]. Hence, ZM-2 has the smallest arc radius of all composite materials, indicating that it has the fastest photogenerated carrier transfer process.

Photoluminescence (PL) spectra were investigated to measure the migration kinetics of light-induced charge carriers. For samples, PL emission spectra were acquired at a wavelength of excitation equivalent to 300 nm. The ZM-2 composite has the lowest PL intensity among all the composites (Fig. 4a). This indicates that the electron-hole complexation in the heterostructure is greatly suppressed, which is due to the strong interaction between ZIS and MnS. In conclusion, it has been demonstrated that the composite ZM-2 is most effective in separating and transferring photogenerated carriers, which facilitated photocatalytic water splitting performance.

Optical properties of various materials were investigated using UV–vis diffuse reflection spectra (UV–vis DRS). Compared to the MnS, in the visible light range, the ZM-2 materials had a wide absorption, with a red-shifted absorption edge compared to ZIS (Fig. 4b). The optical absorption indicated that ZM-2 composite can greatly improve the optical absorption ability to harvest visible light, thus promoting enhanced photocatalysis in the visible region. Using the Kubelka-Munk formula, the data from the DRS was calculated to produce the Tauc plot. The bandgaps of MnS, ZIS and ZM-2 were investigated by means of the Tauc plot (Fig. 4c), showing that correspond to 2.02, 2.49 and 2.44 eV, respectively. We tested the semiconductor types of ZIS and MnS using the Mott-Schottky (M-S) plots in Figs. 4d and e. The $ZnIn_2S_4$ and MnS photocatalysts are n-type and p-type semiconductors, respectively, because of the difference in the curve characteristics (positive/negative slopes), which is in agreement with previous reports [47]. From the M-S plot, the flat band potentials (E_{fb}) of ZIS and MnS were −0.48 and 0.52 eV (*vs.* Ag/AgCl), and the E_{fb} values calculated to be −0.28 and 0.72 eV (*vs.* NHE) *via* the Nernst equation: $E_{NHE} = E_{Ag/AgCl} + 0.197$ [48]. Usually, E_{fb} is positive by 0.3 eV over conduction band (CB) for n-type semiconductors, and valance band (VB) is 0.3 eV higher than E_{fb} for p-type semiconductors [49]. Consequently, the CB of ZIS and VB of MnS are −0.58 and 1.02 eV (*vs.* NHE), respectively. Based on the Tauc and band gap values, the VB of ZIS and CB of MnS are 1.91 and −1.00 eV, respectively. The electron band structure of MnS and ZIS is shown in Fig. S8 (Supporting information). In addition, the produced h$^+$ was detected by ESR. The three peaks observed in Fig. 4f indicated the presence of TEMPO, which is oxidized to TEMPO$^+$ when holes are generated, so the decrease in the peak intensity of the signal indicates the generation of h$^+$ [50–52]. The intensity of the TEMPO peaks decayed because of the increase in light time, which indicates the generation of holes. That is, a lot of amounts of h$^+$ was produced in ZM-2 under visible light.

To further understand the mechanism of photocatalytic hydrogen production, we have intuitively investigated the interfacial interaction and charge transfer mechanism of the two-dimensional $ZnIn_2S_4$/MnS composite photocatalysts using DFT calculations. The work function (Φ), which is derived as $\Phi = E_v$ - E_F, where E_v and

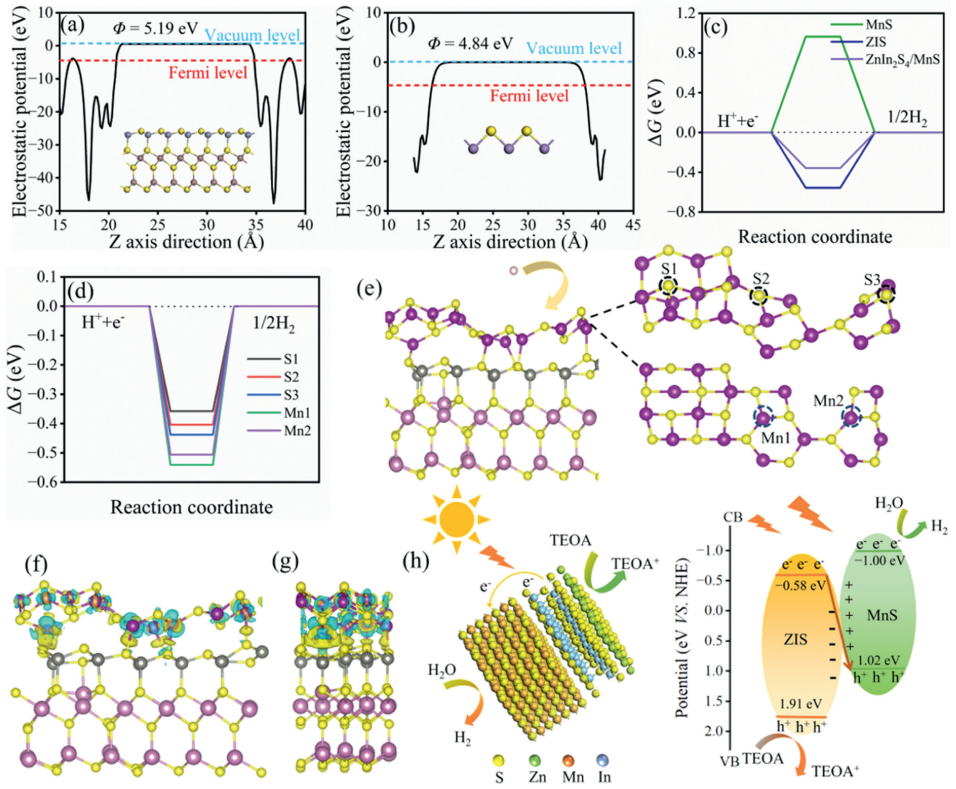

Fig. 5. Calculated electrostatic potentials of (a) ZIS and (b) MnS. (c) Hydrogen-binding free energy (ΔG_{H^*}) of ZIS, MnS and $ZnIn_2S_4$/MnS. (d, e) Hydrogen-binding free energy (ΔG_{H^*}) at Mn-S bonds in the case of hydrogen transition state. (f) Difference in charge density of the optimal structural model. (g) Image corresponding to the longitudinal segment. (h) Schematic representation of the charge transfer channel of ZM-2.

E_F stand for the vacuum energy potential and Fermi energy potential, respectively, is a crucial measure of interfacial charge transfer. The work functions of the MnS (220) and ZIS (102) surfaces were calculated using DFT. The configurations of the MnS (220) and ZIS (102) surfaces used for the calculations are shown in Figs. 5a and b. From the calculation, the work function of ZIS ($\Phi = 5.2$ eV) is higher than that of MnS ($\Phi = 4.8$ eV). As the difference in the electric field in a particular direction, the electrons at the interface will flow from MnS to ZIS until the electric field reaches a balance [53]. When they come into contact, the negative charge located on MnS tends to move towards ZIS. On this basis, a built-in electric field can be generated to achieve efficient separation of photogenerated carriers [54]. *In situ* XPS experiments (Fig. S9 in Supporting information) were carried out on the ZM-2 composites to demonstrate the direction of photoelectron transfer. Compared with ZM-2 under dark conditions, the S 2p, Zn 2p and In 3d peaks shifted positively in the light, while the Mn 2p peak shifted negatively. The binding energy shift under light irradiation indicates that the photogenerated electrons in the CB of ZIS migrate to the VB of MnS [55], which is consistent with the electron movement direction in the S-scheme heterojunction. In the process of photocatalytic reaction, the presence of an internal electric field speeds up the movement of photogenerated electrons from the CB of ZIS to the VB of MnS, which facilitates the photocatalytic hydrogen production. In addition to the DFT calculations, the working functions of ZIS and MnS were also computed by ultraviolet photoemission spectroscopy (UPS). Figs. S10a and b (Supporting information) present the UPS spectra of ZIS and MnS. When the Fermi energy level is 0, the working functions for ZIS and MnS were calculated as 4.15 and 3.63 eV respectively, based on the formula $\Phi = h\nu$ - ($E_{cut\ off}$ - E_F), where $h\nu$ is the incident photon energy (21.22 eV) [56]. Based on the UPS results, it can be concluded that the work function of ZIS is significantly larger than that of MnS, which is in line with the DFT calculations. In addition, the valence bands of ZIS and MnS with respect to NHE are 2.13 V and 1.14 V [57], respectively, which are close to the results of the M-S plots.

The density of states (DOS) for MnS, ZIS, and ZM-2 are shown in Figs. S11a–c (Supporting information), respectively. The valence band of MnS is consists mainly of d orbitals in Fig. S11a, whereas the conduction band consists mainly of p and d orbitals. For ZIS, the valence band is primarily generated by the p and d-orbitals contribution, whereas the conduction band is generated by the s, p, and d-orbital contribution (Fig. S11b). In Fig. S11c, it can be derived that there is some coincidence of Mn and S near the Fermi energy level, and this demonstrates that there may be some bonding interactions between Mn and S [58]. In contrast, the DOS of Zn is mainly concentrated below the Fermi energy level, with less overlap with the DOS distributions of Mn and S, which may imply that the bonding interactions between Zn and Mn and S are weak. Overall, there is a strong bonding relationship between Mn and S in the composites. In addition, as shown in Fig. S11c, the DOS intensity of the $ZnIn_2S_4$/MnS heterojunction decreases near the Fermi energy level, indicating that the carrier recombination is suppressed, which is favorable for photocatalytic hydrogen production [59].

We have investigated the hydrogen evolution reaction pathway of hydrogen in $ZnIn_2S_4$/MnS using DFT calculations and identified the optimal active site in the photocatalytic hydrogen production reaction. The Gibbs free energy (ΔG) of intermediate state in HER indicates H* adsorption/desorption ability, which is a vital indicator of HER performance. As demonstrated in Fig. 5c, the calculations show that $ZnIn_2S_4$/MnS has the lowest $\Delta G = -0.358$ eV compared to other materials, which means that $ZnIn_2S_4$/MnS has the best adsorption/desorption capacity for hydrogen. On the flanks of metal sulphides, metal edges consisting of incompletely coordinated S atoms as well as different metal atoms with metallic prop-

erties and high d electron densities can be used as active sites in photocatalysis, which improves the rate of electron transfer [60]. This study focused on Mn-S bonds at the interface (S1, S2, S3, Mn1 and Mn2) in MnS (Figs. 5d and e). Two types of edges, S edges and Mn edges, can be found in MnS nanosheets. The ligand-unsaturated S and Mn atoms act as photocatalytic active centers, thus promoting hydrogen production. Furthermore, when the active sites of the metal sulphide are in solution, they still have an excellent to bind H^+ in solution, which can reduce the overpotential or activation barrier for H_2 evolution [61]. Remarkably, the energy barrier for adsorbed for H^* intermediates (ΔG_{H^*}) at the S1 site of the Mn-S bond (−0.358 eV) is clearly lower than at other sites, indicating that the S1 site exhibits higher activity in HER. This proves that electrons on MnS smoothly transfer to the ZIS *via* the Mn-S bond, this promotes the transport of charge carriers.

Electron transfer patterns at the interface between two phases were observed using DFT. Fig. 5f displays the charge density variation map of the composite material, where the yellow area represents the region of electron acquisition and the green area signifies the region of electron depletion. The ZIS surface is dominated by the yellow area, meanwhile the MnS side is mainly in the green area, which indicates that the electrons are concentrated in the ZIS side of the composite. In addition, the longitudinal profile image can visualize the electron migration trend from MnS to ZIS more intuitively (Fig. 5g). Therefore, ZIS demonstrates a negative charge, whereas MnS presents a positive charge, resulting in the establishment of an internal electric field between ZIS and MnS. This interface charge transfer is also in good accordance with the shift of the aforementioned XPS peaks.

Summarizing the analytical data and the results of the DFT calculations, a schematic diagram explaining the possible photocatalytic mechanism is given in Fig. 5h. To sum up, the S-scheme heterojunction between MnS and ZIS is confirmed by the results of DFT, UPS and *in situ* XPS analysis. When $ZnIn_2S_4$ is in contact with MnS, an internal electric field is generated due to the movement of electrons, and under visible light irradiation (≥420 nm), electrons migrate from $ZnIn_2S_4$ to MnS, while the presence of the internal electric field inhibits the movement of electrons from the CB of MnS to the CB of $ZnIn_2S_4$, forming a S-scheme heterojunction. A S-scheme charge transfer system was formed by bringing MnS and ZIS into close contact through a hydrothermal reaction. This allows more efficient utilization of carriers and prevents the photo corrosion of ZIS by inhibiting the complexation of ZIS electrons and holes, and is able to retain most of the reduced electrons in ZM-2 for photo-hydrogen production, thus significantly improving the photocatalytic activity.

In summary, the regulation of the sulfur-edge and metal-edge sites *via* the formation of $ZnIn_2S_4$/MnS heterojunctions demonstrated an effective way to enhance the catalytic performance for the production of hydrogen under visible light irradiation. The results indicated that the ZM-2 photocatalyst had the highest hydrogen production rate of 7.95 mmol g^{-1} h^{-1}, up to 4.7 times more than that of ZIS. DFT calculations and *in situ* XPS analysis yielded that the tight contact between MnS and ZIS constitutes a S-scheme heterojunction. The presence of Mn-S bonds *via* the respective sulfur-edge and metal-edge sites in ZIS and MnS components promoted faster charge transfer, significantly enhancing hydrogen evolution performance. Additionally, the surface of MnS contains unsaturated S atoms which act as strong H^+ binding active sites, thus lowering the activation barrier or overpotential for H_2 evolution.

Declaration of competing interest

The authors declare that they have no known competing financial interests or personal relationships that could have appeared to influence the work reported in this paper.

CRediT authorship contribution statement

Yueting Ma: Writing – original draft, Investigation, Data curation, Conceptualization. **Zhiyan Feng:** Validation, Software. **Yuxin Dong:** Validation, Data curation. **Zhiyong Yan:** Writing – review & editing, Supervision. **Hou Wang:** Writing – review & editing, Supervision. **Yan Wu:** Writing – review & editing, Supervision, Resources, Methodology, Funding acquisition.

Acknowledgments

The authors gratefully acknowledge the National Nature Science Foundation of China (No. 22108069) and Natural Science Foundation of Hunan Province, China (No. 2021JJ40260) for the financial support.

Supplementary materials

Supplementary material associated with this article can be found, in the online version, at doi:10.1016/j.cclet.2025.110922.

References

[1] Z. Wei, J. Liu, W. Shangguan, Chin. J. Catal. 41 (2020) 1440–1450.
[2] Y.S. Ouyang, Y. Jiang, S. Ni, et al., ACS Appl. Mater. Interfaces 15 (2023) 32329–32340.
[3] W.K. Chong, B.J. Ng, X.Y. Kong, et al., Appl. Catal. B: Environ. 325 (2023) 122372.
[4] X. Zheng, L. Feng, Y. Dou, et al., Angew. Chem. Int. Ed. 15 (2021) 13209–13219.
[5] S. Zhang, G. Zhang, S. Wu, et al., J. Colloid Interface Sci. 650 (2023) 1974–1982.
[6] A. Alamiery, ChemPhysMater 3 (2023) 64–73.
[7] X. Zheng, Y. Song, Y. Liu, et al., Coord. Chem. Rev. 475 (2023) 214898.
[8] Y. Wu, Y. Qi, G. Zhou, et al., Int. J. Hydrogen Energy 72 (2024) 179–188.
[9] S.B. Wang, Y. Wang, S.L. Zhang, et al., Adv. Mater. 31 (2019) 1903404.
[10] Z. Xiong, Y.D. Hou, R.S. Yuan, et al., Acta Phys. Chim. Sin. 38 (2022) 1903404.
[11] S. Wang, B.Y. Guan, X. Wang, X.W.D. Lou, J. Am. Chem. Soc. 140 (2018) 15145–15148.
[12] C. Li, H. Che, Y. Yan, et al., Chem. Eng. J. 398 (2020) 125523.
[13] J. He, G. Zhang, Y. Jiang, et al., Prog. Nat. Sci.: Mater. 33 (2023) 607–615.
[14] W. Zhang, S. Zhao, Y. Xing, et al., Chem. Eng. J. 442 (2022) 136151.
[15] S. Zhang, Y. Yang, Y. Zhai, et al., Chin. Chem. Lett. 34 (2023) 107652.
[16] V.N. Pham, S. Lee, D.T. Hoang, et al., Inorg. Chem. 62 (2023) 12913–12919.
[17] Y. Geng, X. Zou, Y. Lu, L. Wang, Int. J. Hydrogen Energy 47 (2022) 11520–11527.
[18] H. Fang, J. Cai, H. Li, et al., ACS Appl. Energy Mater. 5 (2022) 8232–8240.
[19] S. Liu, Y. Mao, Z. Su, et al., Catal. Sci. Technol. 13 (2023) 3351–3357.
[20] X. Ren, J. Shi, R. Duan, et al., Chin. Chem. Lett. 33 (2022) 4700–4704.
[21] H. Song, L. Wei, C. Chen, et al., J. Catal. 376 (2019) 198–208.
[22] X. Fang, L. Cui, T. Pu, et al., Appl. Surf. Sci. 457 (2018) 863–869.
[23] C. Ouyang, W. Huang, H. Tang, et al., ACS Appl. Energy Mater. 5 (2022) 12739–12751.
[24] X. Wang, X. Wang, J. Huang, et al., Nat. Commun. 12 (2021) 4112.
[25] B. Zhu, W. Fu, J. Qu, et al., Chem. Eng. J. 497 (2024) 154712.
[26] J. Song, Y. Chen, H. Huang, et al., Adv. Sci. 9 (2022) 2104522.
[27] J. Wang, X. Niu, Q. Hao, et al., Chem. Eng. J. 493 (2024) 152534.
[28] Y. Qi, G. Zhou, Y. Wu, et al., J. Colloid Interface Sci. 664 (2024) 107–116.
[29] Z. Jin, T. Wei, J. Huang, et al., Int. J. Hydrogen Energy 45 (2020) 22711–22721.
[30] G. Li, H. Liang, X. Fan, et al., J. Mater. 11 (2023) 14809–14818.
[31] Y. Liu, L. Li, J. Zhu, et al., ACS Appl. Mater. Interfaces 10 (2018) 27911–27919.
[32] A.M.A. Omar, H.S.H. Mohamed, G. Khabiri, Sep. Purif. Technol. 339 (2024) 126712.
[33] S.H. Chen, X.Y. Xiao, P.H. Li, et al., Environ. Sci. Nano 7 (2020) 753–763.
[34] M. Tan, Y. Ma, C. Yu, et al., Adv. Funct. Mater. 32 (2021) 2111740.
[35] G. Zhang, D. Chen, N. Li, et al., Appl. Catal. B: Environ. 232 (2018) 164–174.
[36] Y. Xiao, H. Wang, Y. Jiang, et al., J. Colloid Interface Sci. 623 (2022) 109–123.
[37] J.J. Li, W. Li, Z.F. Liu, et al., ACS Appl. Nano Mater. 6 (2023) 16927–16937.
[38] T. Gao, Y. Li, J. Tian, et al., J. Alloys Compd. 951 (2023) 169939.
[39] Z.Y. Peng, Y.H. Jiang, X.Q. Wang, et al., Ceram. Int. 45 (2019) 15942–15953.
[40] Z. Huang, P. Sun, H. Zhang, et al., ACS Catal. 14 (2024) 4581–4592.
[41] S. Liu, D. Chi, R. Chen, et al., Renew. Energy 219 (2023) 119494.
[42] L. Yi, R. Zhu, H. Jiang, G. Zhang, Sep. Purif. Technol. 349 (2024) 127885.
[43] M. Tan, Y. Ma, C. Yu, et al., Adv. Funct. Mater. 32 (2021) 2111740.
[44] V.N. Rao, N.L. Reddy, V. Preethi, et al., Int. J. Hydrogen Energy 48 (2023) 11754–11774.
[45] X. Li, W. Bi, L. Zhang, et al., Adv Mater. 28 (2016) 2427–2431.
[46] H.S. Moon, K.C. Hsiao, M.C. Wu, et al., Adv. Mater. 35 (2023) e2200172.
[47] R. Wang, W. Yu, N. Fang, et al., Appl. Catal. B: Environ. 341 (2024) 123284.
[48] H. Wang, J. Liu, X. Xiao, et al., Chin. Chem. Lett. 34 (2023) 107125.
[49] W.J. Ong, L.K. Putri, Y.C. Tan, et al., Nano Res. 10 (2017) 1673–1696.
[50] Z. Sun, X. Yang, X.F. Yu, et al., Appl. Catal. B: Environ. 285 (2021) 119790.
[51] Z. Shi, W. Chen, Y. Hu, et al., Molecules 29 (2024) 1362.

[52] Z. Chen, M. Li, Y. Cui, Y. Wang, Mater. Today Sustainability 24 (2023) 100591.
[53] H. Wang, Y. Sun, Y. Wu, et al., Appl. Catal. B: Environ. 245 (2019) 290–301.
[54] L. Wang, G. Tang, S. Liu, et al., Chem. Eng. J. 428 (2022) 131338.
[55] C. Qin, Y. Yang, G. Zhou, et al., Chem. Eng. J. 487 (2024) 150571.
[56] J. Huang, B. Chai, J. Xiao, et al., Chem. Eng. J. 481 (2024) 148501.
[57] X. Wang, T. Shi, X. Wang, et al., J. Energy Chem. 92 (2024) 151–161.
[58] C.H. Shen, X.J. Wen, Z.H. Fei, et al., J. Colloid Interface Sci. 579 (2020) 297–306.
[59] Q. Zhang, H. Gu, X. Wang, et al., Appl. Catal. B: Environ. 298 (2021) 120632.
[60] W. Tu, Y. Li, L. Kuai, et al., Nanoscale 9 (2017) 9065–9070.
[61] M. Xiong, B. Chai, J. Yan, et al., Appl. Surf. Sci. 514 (2020) 145965.